

RSC Advances



This is an *Accepted Manuscript*, which has been through the Royal Society of Chemistry peer review process and has been accepted for publication.

Accepted Manuscripts are published online shortly after acceptance, before technical editing, formatting and proof reading. Using this free service, authors can make their results available to the community, in citable form, before we publish the edited article. This *Accepted Manuscript* will be replaced by the edited, formatted and paginated article as soon as this is available.

You can find more information about *Accepted Manuscripts* in the [Information for Authors](#).

Please note that technical editing may introduce minor changes to the text and/or graphics, which may alter content. The journal's standard [Terms & Conditions](#) and the [Ethical guidelines](#) still apply. In no event shall the Royal Society of Chemistry be held responsible for any errors or omissions in this *Accepted Manuscript* or any consequences arising from the use of any information it contains.



Porous three-dimensional activated reduced graphene oxide as anode materials for lithium ion batteries

Xianjun Zhu,^{*a} Linwen Zuo,^a Shuilin Wu,^b Xiaodi Qu,^a Meng Wei,^a Li He,^a Yu Zhong^a and Yanwu Zhu^{*b}

Received 00th April 2016,
Accepted 00th April 2016

DOI: 10.1039/x0xx00000x

www.rsc.org/

A porous reduced graphene oxide, with a Brunauer-Emmett-Teller surface area of up to $\sim 3100 \text{ m}^2 \text{ g}^{-1}$, is prepared by using chemical activation of microwave exfoliated graphite oxide. The sp²-bonded carbon has a continuous three-dimensional network of highly curved atom-thick walls with ~ 1 to 5 nm width pores. As an anode material for lithium ion battery, it can deliver a reversible specific capacity of $\sim 1600 \text{ mAh g}^{-1}$. To understand the Li storage mechanism, the porous carbon samples with specific surface area tunable were investigated. The high reversible capacity indicates that the meso- and micropores are the key factor for Li insertion/extraction during discharge and charge. The porous structure and large specific surface area is believed to have contributed to the high performance.

INTRODUCTION

Energy storage has become more demanded because of the fast-growing market of portable electronic devices and hybrid electronic vehicles (HEVs).¹⁻³ Li ion batteries (LIBs) are attractive electrochemical energy storage devices. They are considered as the leading candidates for hybrid, plug-in hybrid as well. The development of Li ion batteries mainly relies on the development of long life, fast charging-discharging, and large capacity electrode materials.

Graphite is a widely commercial carbon material as an anode material for Li ion batteries owing to its high Coulombic efficiency and acceptable specific capacity by forming interaction (LiC_6) which has a theoretical specific capacity of 372 mAh g^{-1} .⁴ For disordered carbon materials, Sato and co-workers proposed a Li_2 covalent molecule model where each Li atom is trapped in one hexagonal ring (called a "covalent" site) and predicted the highest Li storage capacity of 1116 mAh g^{-1} (LiC_2).⁵ As the specific capacity of Li ion batteries is strongly affected by carbon electrodes, other carbon-based materials have been studied as high capacity electrodes, but show only a limited enhancement of storage capacities ($400\sim 700 \text{ mAh g}^{-1}$).⁶⁻¹¹ Although the model is controversial, a host of extra storage sites would be expected in carbonaceous nanostructures to create a higher specific capacity.

Graphene, thanks to its large surface to mass ratio exceeding $2600 \text{ m}^2 \text{ g}^{-1}$, with high electrical conductivity and high

mechanical strength, is a promising material for electrodes in LIBs.¹²⁻¹⁴ According to the Li_2 covalent molecule model, the interlayer spacing (d_{002}) of carbon materials is a key parameter which need be large enough ($\sim 4.0 \text{ \AA}$).¹⁵ Additionally, Pan clarified that the disorder/defects in graphene nanosheets is another key structural parameters to affect the Li storage properties ($1013\sim 1054 \text{ mAh g}^{-1}$).^{9,16} To date, the best anodes with chemically modified graphene (CMG) have reached specific capacity of $\sim 1200 \text{ mAh g}^{-1}$ in a half cell. This fact indicates that, besides the interlayer spacing and disorder/defects, there must be other key parameters that affect the storage capacity.¹⁷⁻¹⁹

Recently, a graphene-derived carbon with extremely high surface area of up to $\sim 3100 \text{ m}^2 \text{ g}^{-1}$ has been reported by us, which was prepared by microwave irradiation of graphite oxide (GO) followed by chemical activation with potassium hydroxide (KOH).²⁰ This activated microwave-expanded graphite oxide (aMEGO) has a large fraction of meso- and micropores that provide a large and accessible surface area for charge accommodation and therefore improve specific capacitance to achieve a relatively high gravimetric energy density.^{20,21}

Inspired by the above, in this study, we investigated aMEGO materials with specific surface area (SSA) tunable to apply in LIBs as anode materials. Through comparative experiments, we found that meso- and micropores may play a key role in the capacity enhancement of graphene nanosheets. Importantly, the sample with SSA $\sim 3120 \text{ m}^2 \text{ g}^{-1}$ can reach a reversible specific capacity of 1603 mAh g^{-1} , which is the highest value up to now. The reversible Li storage capacity of pure graphene nanosheets can be enhanced by introducing a host of meso- and micropores rather than by expanding interlayer spacing and disorder/defects shown in the literatures.^{9,16}

^a College of Chemistry, Central China Normal University, 152 Luoyu Rd, Wuhan, Hubei 430079, China. E-mail: xjzhu@mail.ccnu.edu.cn

^b Department of Materials Science and Engineering & CAS Key Laboratory of Materials for Energy Conversion, University of Science and Technology of China, 96 Jin Zhai Rd, Hefei, Anhui 230026, China. E-mail: zhuyanwu@ustc.edu.cn

† Electronic Supplementary Information (ESI) available. See DOI: 10.1039/x0xx00000x

EXPERIMENTAL SECTION

Synthesis of activated microwave exfoliated graphite oxide (aMEGO)

The synthesis of activated graphene was achieved by the method previously described.²⁰ It involved the following steps in sequence. (i) preparation of graphite oxide (GO) (ii) microwave irradiation to prepare microwave exfoliated graphite oxide (MEGO), and (iii) activation of MEGO with potassium hydroxide. Briefly, GO powders made from the modified Hummers' method were irradiated in a domestic microwave oven operated at 1100 W for ~30 seconds. During the irradiation, a large volume expansion of the GO powder occurred, and the black, fluffy MEGO powder obtained was collected for activation. Typically, 400 mg MEGO powder was dispersed in 20 ml 7M aqueous KOH solution and stirred for 4 hours at a speed of 400 rpm, followed by another 20 hours of static soaking in ambient conditions. The extra KOH solution was removed by briefly filtering the mixture through a polycarbonate membrane (Whatman, 0.2 μm); then the mixture was dried in the lab environment at 80 °C for 24 hours. A KOH to MEGO ratio was calculated by assuming the MEGO in the dry KOH/MEGO mixture gave the same mass yield.

It was found that the KOH uptake (KOH/MEGO ratio) was linearly dependent on the molarity of the KOH solution. The mass ratio of KOH to MEGO was varied to be 4:1, 6:1, 8:1, and 10:1 to control the specific surface area of activated graphene. In the activation process, the dry precursor KOH/MEGO was first heated at 350 °C for 30 minutes, the temperature was ramped at 5 °C min⁻¹ to 800 °C and held there for 1 hour in a horizontal tube furnace, with an argon flow of 150 sccm at a vacuum pressure of 400 Torr. After cooling down in vacuum, the sample was repeatedly washed by deionized water until a pH value of 7 was reached. Then the sample was dried at 80 °C in ambient for 2 hours, followed by thermal annealing at 800 °C in vacuum (0.1 Torr) for 2 hours, to generate 'activated MEGO' (aMEGO) powders. For comparison, a control MEGO sample without KOH activation was also prepared at the same experimental condition (donated as T-MEGO).

Characterizations

The structure of the as-prepared samples was characterized by X-ray diffraction (XRD, CuK α radiation; $\lambda=0.15414$ nm) at the scan rate of 2° min⁻¹ in the 2 θ range of 5 and 80°. Scanning electron microscopy (SEM) was performed using JSM-6700F (field emission gun; specimen chamber pressure of about 10–5 Pa; accelerating voltage 10 kV; working distance 8 mm). Transmission electron microscopy (TEM, JEM - 2010F; 200 keV) was used to study the morphology and microstructure of the composites. Raman spectrum measurements were carried out using INVIA (RENISHAW, England) system with a 514.5 nm wavelength incident laser light.

X-ray photoelectron spectroscopy (XPS) analysis was performed using a Kratos AXIS Ultra DLD XPS equipped with a 180° hemispherical energy analyzer. Photoelectron was stimulated by monochromated Al K α radiation (1486.6 eV)

with an operating power of 150 W. It was operated in the analyzer mode at 80 eV for survey scans and 20 eV for detailed scans of core level lines.

The pore structure of the sample was investigated using physical adsorption of nitrogen at the liquid-nitrogen temperature (77 K) on an automatic volumetric sorption analyzer (NOVA2000, Quantachrome). Prior to measurement, a sample was vacuum-degassed at 120 °C for 16 h. The specific surface area (SSA) was determined according to the Brunauer–Emmett–Teller (BET) method in the relative pressure range of 0.05 ~ 0.2.

Electrochemical Characterizations

Electrochemical experiments were performed using 2032 coin-type cells. The working electrode consisted of 95 wt% as-prepared active material and 5 wt% polytetrafluoroethylene binder. The electrolyte was a solution of 1 M LiPF₆ in EC/DEC (1:1 by volume). Pure Li foil was used as the counter electrode and the separator was Celgard 2300. The cells were discharged and charged galvanostatically in a voltage window from 0.005 to 3.0 V using a Land battery tester (China) at room temperature.

RESULTS AND DISCUSSION

As shown in Fig. 1, the synthesis process for aMEGO materials is as follows. First, GO was prepared by a modified Hummers' method. Then, these GO sheets were irradiated in a microwave oven, which led to a degree of deoxygenation and a large volume expansion to yield black and fluffy powders composed of microwave-expanded graphite oxide (denoted as MEGO). Finally the as-made MEGO powder was placed in KOH solution with different concentrations for KOH chemical adsorption, then filtrating and drying to form a series of KOH/MEGO mixtures. Each KOH/MEGO mixture was put in a tube furnace under flowing argon at 400 Torr and heated at 800 °C for 1 hour, yielding activated microwave-exfoliated graphite oxide powders (donated as aMEGO, See experimental section for further details of material preparation).

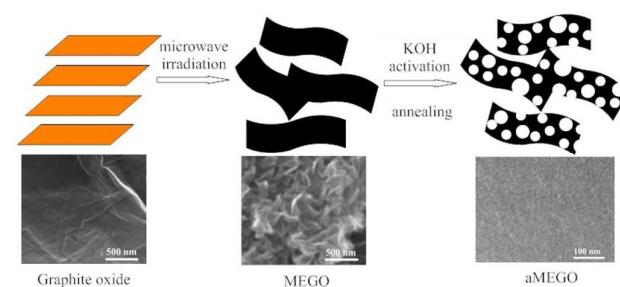


Fig. 1 Scheme for preparing aMEGO samples.

The KOH activation generated nanoscale pores in the aMEGO sheets. The SSA of the aMEGO can be readily controlled by the ratio of KOH/MEGO. In this work, 4 kinds of aMEGO materials were prepared, whose mass ratios of KOH/MEGO are 4, 6, 8

and 10 respectively (denoted as aMEGO-1, 2, 3 and 4, respectively). The morphology of a typical aMEGO sample (aMEGO-4) was observed by scanning electron microscopy (SEM) and is shown in Fig. 2a and b. SEM image shows that aMEGO is porous. Fig. 2c and d shows the high-resolution TEM (HR-TEM) images of the microstructure, which has a substantial amount of meso- and micro- pores in the aMEGO sheets. The activation with KOH yields a continuous 3D network of meso- and micro- pores of extremely small size. The overstructure consisted of meso- and micro- pores with an interconnected network, would be expected to provide large SSA.

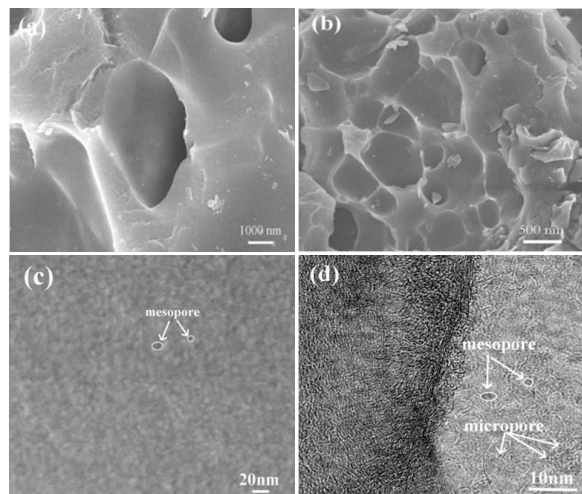


Fig. 2 SEM images of the aMEGO-4 sample (SSA $\sim 3120 \text{ m}^2 \text{ g}^{-1}$) (a) at low-magnification, (b) at high-magnification. High-resolution TEM images of the aMEGO-4 sample (c) at low-magnification, (d) at high-magnification.

The structure changes from graphite to aMEGO were investigated by X-ray diffraction (XRD, Supporting information Fig. S1). The XRD patterns of graphite exhibits a characteristic (002) peak at 26.55° , corresponding to the interlayer distance $d=0.335 \text{ nm}$. After oxidation, the (002) peak of graphite disappears and an additional peak at $2\theta=10.44^\circ$ is observed, which corresponds to the (001) diffraction peak of GO ($d=0.86 \text{ nm}$), indicating the complete oxidation of graphite. This is a prerequisite to successfully exfoliating graphite oxide and obtaining porous 3D single-layer or few-layer graphene oxide sheets. After microwave irradiation for GO, there are very low intensity characteristic peaks (002) at 23.5° and (100) at 43.6° for MEGO. aMEGO and T-MEGO samples have similar characteristic peaks with those of MEGO, indicating that either all stacking of graphene layers in aMEGO is lost, or any remaining stacking is disordered, compared to those of graphite and GO.²²

Raman spectra have been proved to be an essential tool to characterize carbon materials.^{23, 24} The Raman spectra of graphite, GO and aMEGO have different characteristic peaks (Supporting information Fig. S2). In the spectrum of graphite, a prominent G band at 1580 cm^{-1} corresponds to an ordered E_{2g} mode of graphite and is related to the vibration of sp^2 -bonded

carbon atoms. For GO, the G band shifts to 1596 cm^{-1} , and a new peak (the D band) appears at 1358 cm^{-1} , which is ascribed to edges, other defects, and disordered carbon. The appearance of the D band arises from the destruction of the E_{2g} symmetry and structural distortion of sp^2 domains, indicating that the GO nanosheets become highly disordered due to the oxidation of graphite. After microwave irradiation, the D band is located at $\sim 1352 \text{ cm}^{-1}$, and the G band at $\sim 1590 \text{ cm}^{-1}$. Nevertheless, the disordered D band is stronger than the ordered G band. It can be seen that the intensity ratio of I_D/I_G increases from 0.94 for GO to 1.10 for aMEGO. This phenomenon can be attributed to the significant decrease of the size of the in-plane sp^2 domains, and the increase of highly disordered structure of aMEGO nanosheets.²⁵

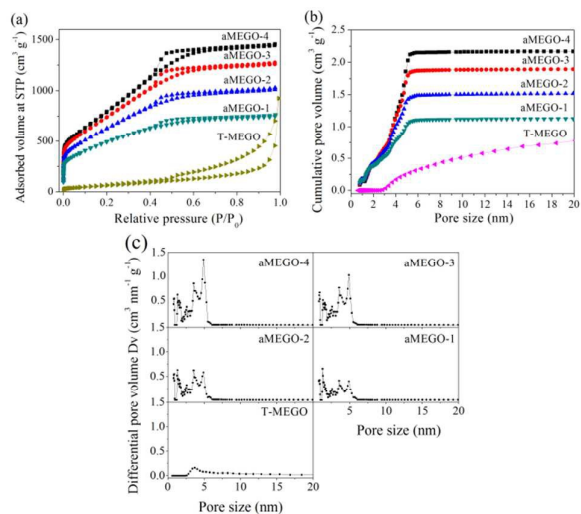


Fig. 3 Nitrogen adsorption/desorption analysis of the aMEGO samples. (a) Isotherms of aMEGO samples with different ratios of KOH/MEGO, (b) Cumulative pore volume and (c) Pore size distribution calculated using a slit/cylindrical NLDFT model of aMEGO samples with different ratios of KOH/MEGO.

The porosity of aMEGO samples was analyzed by nitrogen adsorption-desorption measurement. Fig. 3a shows the characteristic isotherms of various aMEGO samples with different ratios of KOH/MEGO. The nitrogen adsorption below the relative pressure of $P/P_0=0.1$ is a feature of micropore filling. The continuous rise of the isotherms in the relative pressure ranged from 0.1 to 0.4 combined the decreased slope above 0.4 implied the presence of an appreciable amount of mesopores. Additionally, the result also shows that the aMEGO-4 sample with high ratio of KOH/MEGO has more meso- and micropores than that with low ratio of KOH/MEGO (aMEGO-1, 2, or 3), indicating that aMEGO-4 should have larger SSA. Fig. 3b shows the result of the cumulative pore and pore size analysis. The pore size calculated by applying the nonlocal density functional theory (NLDFT) method assuming a slit geometry for the micropores and a cylindrical pore geometry for the mesopores indicates the existence of well-defined micro- and mesopores with sizes of less than 5 nm. Brunauer-Emmett-Teller (BET) for aMEGO-4 is as high as $3120 \text{ m}^2 \text{ g}^{-1}$ with a total volume of $2.16 \text{ cm}^3 \text{ g}^{-1}$, which is even higher than the

theoretical limit of graphene.²⁰ For aMEGO-1, 2, and 3 samples, their SSA are 1805, 2373 and 2852 m² g⁻¹, respectively. It was noted that the SSA of aMEGO samples increases with the ratio of KOH/MEGO. When the ratio is more than 8, the SSA keeps almost constant.²⁰ The pore size/volume distribution indicates that the aMEGO sample is distinctive due to the existence of well-defined meso- and micropores. Fig. 3c shows the micro- and mesopores of the as-prepared aMEGO samples. The main porous scale is under 5 nm, which mainly comes from the pores of KOH activation of MEGO nanosheets. For the MEGO without KOH activation (donated as T-MEGO), there are little meso- and micropores on the surface of graphene from its SEM (Supporting information Fig. S3), whose SSA is only 263 m² g⁻¹.

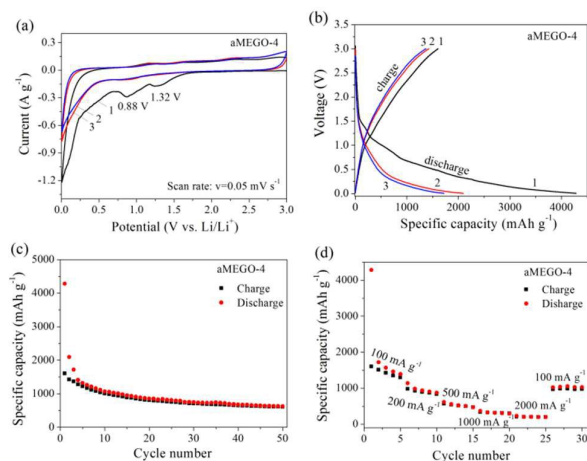


Fig. 4 Electrochemical performance of aMEGO-4 (SSA \sim 3120 m² g⁻¹) sample in 1 M LiPF₆/EC+DEC electrolyte in the potential of 0.005 \sim 3.0 V. (a) CV curve at the scan rate of 0.05 mV s⁻¹. (b) The first three discharge/charge curves at the current density of 100 mA g⁻¹. (c) Cycling performance at the current density of 100 mA g⁻¹. (d) The rate performance at various current densities.

To measure the electrochemical performance of the aMEGO, the aMEGO was mixed with polytetrafluoroethylene (PTFE) in a weight ratio of 95:5 for preparing a working electrode. Fig. 4a shows the cyclic voltammetry (CV) curves of aMEGO-4 sample at a scan rate of 0.05 mV/s in the potential range of 0.005 \sim 3.0 V. In the negative scan, there are two peaks at 1.32 V and 0.88 V respectively, mainly during the first cycle and less pronounced in the following cycles. Below the voltage of 0.7 V, it is the main region for Li to be inserted into the aMEGO nanosheets; in the positive direction, Li will be extracted from the aMEGO, and there are no obvious peaks during Li extraction. After the first cycle, the CV curves are similar except for much capacity fading. As a comparison, for the CV curves of non-porous T-MEGO, there is only one anodic peak around 0.75 V at the first negative scan, which is ascribed to the decomposition of electrolytes and the formation of SEI layer^{26,27}. Its electrochemical performance is worse than that of aMEGO (Supporting information Fig. S4). Therefore, it is suggested that the peak for aMEGO-4 at 1.32 V correspond to the SEI formation on the surface of graphene nanosheets due

to easily arriving for Li, and the peak at 0.88 V correspond to the SEI formation on the surface of meso- and micropores because of hardly arriving for Li.

Fig. 4b shows the discharge and charge curves of aMEGO-4 at a current density of 100 mA/g between 0.005 and 3.0 V vs. Li⁺/Li, whose shapes match well with the CV curves. The first discharge specific capacity of 4282.7 mAh g⁻¹ was achieved, and the reversible specific capacity was 1603.4 mAh g⁻¹, which is more than 4 times that of commercial graphite. Such high reversible capacity might indicate some other lithium storage routes existing in porous aMEGO anode materials except the conventional graphite intercalation mechanism. The large irreversible capacity of 2679.3 mAh g⁻¹ might result from the formation of SEI layer at the surface of aMEGO caused by decomposition of the electrolyte and/or irreversible lithium insertion. aMEGO has a large number of pores activated by KOH, and the high surface area can provide more opportunities for the decomposition of the electrolyte, thus leading to large irreversible capacity and low Coulombic efficiency (37.4%).

For the aMEGO-4 sample, in the first discharge process, the voltage decreases steeply from open circuit voltage (3.1 V) to 1.5 V, and then two short slopes in the ranges of 1.5 \sim 1.2 V and 1.2 \sim 0.7 V respectively, which is different from that of T-MEGO (Supporting information Fig. S4). Another long slope is observed below 0.7 V, yielding a total first discharge capacity of 4282.7 mAh g⁻¹. The voltage above \sim 0.7 V can be mainly attributed to the electrolyte decomposition and SEI film formation on the surface of aMEGO. It is noted that the most part of aMEGO specific capacity falls in the region below 0.7 V in the first discharge step. The capacity below 0.7 V could correspond to the lithium insertion on the basal plane of aMEGO involving in meso- and micropores, and could also be ascribed to the faradic capacity on the surface or on the edge sites of aMEGO.^{16,28,29} Correspondingly, the first charge curve has two slopes up to a capacity of 1603.4 mAh g⁻¹. The first slope at 0.005 \sim 1.0 V is almost a linear, which maybe correspond to the Li desorbed on the large pore surface of aMEGO, and the second slope at 1.0 \sim 3.0 V is a curve, which is due to the Li deinsertion from the meso- and microporous surface of the aMEGO. To the best of our knowledge, the reversible capacity of 1603.4 mAh g⁻¹ is the highest for carbon materials reported to date.²⁷ On the second discharge and charge profiles, there exists a large voltage hysteresis and no distinct voltage plateau, as previously reported.^{9,16,30} The second discharge and charge capacities are 2094.5 and 1424.1 mAh g⁻¹, respectively. From the second cycle on, the discharge and charge curves are similar. Comparatively, the aMEGO samples with different SSA have similar discharge/charge profiles (Supporting information Fig. S5). The first reversible capacities (charged capacities) for aMEGO-1, 2, 3 and 4 are 1085.3, 1307.6, 1419.8 and 1603.4 mAh g⁻¹, respectively, indicating that the reversible capacities increase with SSA. The result indicates that the reversible capacities of the aMEGO samples are all much higher than 372 mAh g⁻¹ of graphite as well as those of the previously reported pure graphene nanosheets and doped graphene nanosheets.³¹⁻³³ However,

the first cycle Coulombic efficiencies decrease with SSA (41.6~37.4 %), and the irreversible capacities increase with SSA correspondingly (1526 ~ 2679 mAh g⁻¹).

Fig. 4c shows the cycling performance of the aMEGO-4 sample. The discharge capacities in the first, 2nd, 10th, 20th, 30th, 40th and 50th cycles are 4282.7, 2094.5, 1070.2, 852.2, 749.2, 676.7 and 625.5 mAh g⁻¹, respectively. It is noted that the discharge capacity of aMEGO-4 drops from 4282.7 mAh g⁻¹ to 2094.5 mAh g⁻¹ with a loss capacity of 2188.2 mAh g⁻¹ after the first cycle. Then the discharge capacity fades slowly. After 50 cycles, the discharge capacity is 625.5 mAh g⁻¹. On the other hand, the reversible capacity (charged capacity) after 50 cycles for aMEGO-4 is 606.5 mAh g⁻¹. aMEGO-4 showed 37.8% retention of the initial charge capacity after 50 cycles, which is the lowest among those of the aMEGO samples (38.2, 38.9 and 41.5% for aMEGO-1, 2 and 3 respectively) (Supporting information Fig. S5). The result indicates that the first discharge/charge capacity increases with SSA and the capacity fading of aMEGO samples also increases with SSA due to the aggregation and restacking of aMEGO nanosheets during discharging and charging. Further improvement can be expected by tuning the size and structure of aMEGO nanosheets or hybridizing with other active materials to prevent aggregating and restacking of aMEGO nanosheets in our future research work.

Fig. 4d shows the rate performance of aMEGO-4 at different current densities. When the current density is increased from 100 to 2000 mA g⁻¹, the discharge capacity is decreased from ~4283 to ~200 mA h g⁻¹ (4.7% retention). The capacity fading is significantly faster than that of T-MEGO. Furthermore, as long as the current reverts back to 100 mA g⁻¹, the capacity of aMEGO-4 is recovered to ~970 mAh g⁻¹, which is higher ~600 mAh g⁻¹ of T-MEGO as well as more than 2 times theoretical capacity 372 mAh g⁻¹ of graphite.

Why does the aMEGO sample have so high capacity? According to the literature,^{16, 5} for nongraphite carbon materials, Sato proposed a Li₂ covalent molecule model where Li is trapped in one hexagonal ring (called a 'covalent' site) and predicted the highest Li storage capacity of 1116.0 mAh g⁻¹ (LiC₂) in comparison with the form LiC₆ of graphite (372 mAh g⁻¹). According to the micropore mechanism, the insertion/extraction of lithium ions from the micropores has to go through the cavities of graphene crystalline. The interaction between lithium atoms and micropores result in an appreciable voltage hysteresis in the discharge and charge process. Our aMEGO sample can deliver 1603.4 mAh g⁻¹ of a specific capacity which is much higher than 1116.0 mAh g⁻¹. By calculation, the reversible capacity of 1603.4 mA g h⁻¹ is equal to have the form of LiC_{1.4} model. In the aMEGO sample with large SSA, besides the single-layer graphene nanosheets, there are numerous meso- and micropores, leading to have a lot of edges/defects. Taking the aMEGO-4 sample into consideration, after the first full discharge, the high-resolution TEM image in Fig. 5a shows that the presence of Li insertion around micro- and mesopores or on the surface of graphene nanosheets is clearly observed. The dark part indicates the presence of Li nanoparticles, which display a single-crystalline structure from

the inlet image of Fig 5a. The lattice spacing of 0.35 nm corresponds to the *d* spacing between adjacent (100) crystallographic planes of cubic Li crystal. Fig 5b shows the binding energy profile of Li for the aMEGO-4 sample at the first full discharge state measured by X-ray photoelectron spectroscopy (XPS). Compared to graphite, the observation of Li_{1s} binding energies at 57.3 eV suggests that some Li-containing groups remain on the surface of aMEGO. So, the high capacity for the aMEGO sample could be mainly ascribed to the following reasons.³⁴ (1) the 3D nanoporous interconnected network possesses the advantages of both nanosized building blocks and microsized assemblies towards lithium storage, resulting in lithium binding/adsorbing /inserting on the so called 'covalent' site. (2) the meso-/microporous graphene nanosheet can act as an efficient buffering and conducting matrix, and it thus improves the electrical conductivity. (3) the different lithiation potentials of meso-/micro- porous graphene give rise to stepwise Li-storage processes during lithium insertion/extraction. Based on this, we suggest that the lithium insertion/extraction of aMEGO is shown in Fig 5c. In the aMEGO sample, there are a lot of meso- and micropores in the graphene nanosheets resulting in large SSA and lots of edges/defects, which is suitable for large reversible lithium storage. It is noted that the meso- and micro-pores is the key factor to affect the specific capacity of graphene nanosheets. Because of its low initial Coulombic efficiency, aMEGO is far from practical application up to now. But we can take its advantage of high SSA and good conductivity to hybrid aMEGO with other electrode materials, such as transition metal oxides, Si et al. The hybrid materials with high initial Coulombic efficiency and improved electrochemical performance can be a good candidate for practical electrode materials.

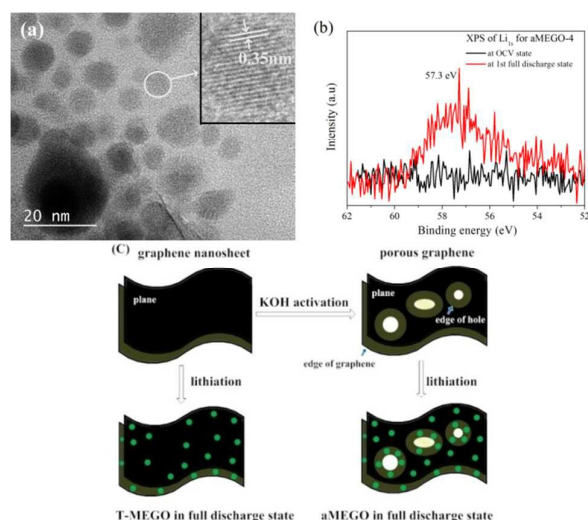


Fig. 5 (a) High-resolution TEM image of the aMEGO-4 sample at the first full discharge state. The presence of Li insertion around micro- and mesopores or on the surface of graphene nanosheets is clearly observed. (b) Li_{1s} binding energy profile measured by XPS at OCV state and at the first full discharge state for the aMEGO-4. (c) Lithiation mechanism of aMEGO as anode materials for LIBs.

Conclusions

In summary, a porous carbon with SSA tunable was prepared via KOH activation of microwave exfoliated graphite oxide. The effects of SSA on Li storage properties were investigated. These carbon samples consist of numerous meso- and micropores sp^2 graphene nanodomains. The enhanced capacity in the carbon samples is mainly ascribed to meso- and micropores in graphene nanosheets to provide additional reversible Li storage sites, such as large surface area, edges/defects. These carbon materials with large SSA may find applications in high-capacity storage materials for advanced lithium ion batteries.

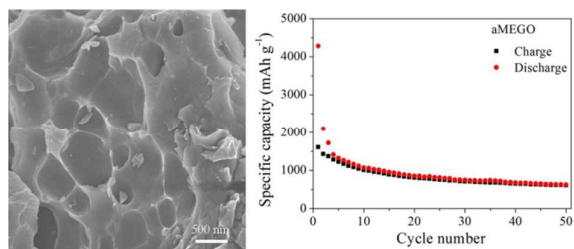
Acknowledgements

This work was supported by the Natural Science Foundation of Hubei Province (No. 2011CDB161). Y. Zhu appreciates the financial support from China Government 1000 Plan Talent Program, China MOE NCET Program, Natural Science Foundation of China (51322204), the Fundamental Research Funds for the Central Universities (WK2060140014 and WK2060140017) and the External Cooperation Program of BIC, Chinese Academy of Sciences (211134KYSB20130017).

Notes and references

- M. Pumera, *Energ. Environ. Sci.*, 2011, **4**, 668.
- A. C. Dillon, *Chem. Rev.*, 2010, **110**, 6856.
- A. S. Arico, P. Bruce, B. Scrosati, J. M. Tarascon and W. Van Schalkwijk, *Nat. Mater.*, 2005, **4**, 366.
- J. R. Dahn, T. Zheng, Y. Liu and J. S. Xue, *Science*, 1995, **270**, 590.
- K. Sato, M. Noguchi, A. Demachi, N. Oki and M. Endo, *Science*, 1994, **264**, 556.
- Y. Wu, S. Fang and Y. Jiang, *J. Power Sources*, 1998, **75**, 201.
- C. Wan Park, S.-H. Yoon, S. I. Lee and S. M. Oh, *Carbon*, 2000, **38**, 995.
- H. Wu and Q. Yang, *Carbon*, 1999, **37**, 1409.
- D. Pan, S. Wang, B. Zhao, M. Wu, H. Zhang, Y. Wang and Z. Jiao, *Chem. Mater.*, 2009, **21**, 3136.
- Y. P. Wu, E. Rahm and R. Holze, *J. Power Sources*, 2003, **114**, 228.
- Y. Wu, C. Jiang, C. Wan and E. Tsuchida, *Electrochem. Commun.*, 2000, **2**, 272.
- F. Bonaccorso, A. Lombardo, T. Hasan, Z. Sun, L. Colombo and A. C. Ferrari, *Materials Today*, 2012, **15**, 564.
- C. Lee, X. Wei, J. W. Kysar and J. Hone, *Science*, 2008, **321**, 385.
- A. K. Geim and K. S. Novoselov, *Nat. Mater.*, 2007, **6**, 183.
- C. Xu, B. Xu, Y. Gu, Z. Xiong, J. Sun and X. S. Zhao, *Energ. Environ. Sci.*, 2013, **6**, 1388.
- E. Yoo, J. Kim, E. Hosono, H.-s. Zhou, T. Kudo and I. Honma, *Nano Lett.*, 2008, **8**, 2277.
- W. Xing, R. A. Dunlap and J. R. Dahn, *J. Electrochem. Soc.*, 1998, **145**, 62.
- M. Winter, J. O. Besenhard, M. E. Spahr and P. Novák, *Adv. Mater.*, 1998, **10**, 725.
- P. Lian, X. Zhu, S. Liang, Z. Li, W. Yang and H. Wang, *Electrochim. Acta*, 2010, **55**, 3909.
- Y. Zhu, S. Murali, M. D. Stoller, K. J. Ganesh, W. Cai, P. J. Ferreira, A. Pirkle, R. M. Wallace, K. A. Cychosz, M. Thommes, D. Su, E. A. Stach and R. S. Ruoff, *Science*, 2011, **332**, 1537.
- L. L. Zhang, X. Zhao, M. D. Stoller, Y. Zhu, H. Ji, S. Murali, Y. Wu, S. Perales, B. Clevenger and R. S. Ruoff, *Nano Lett.*, 2012, **12**, 1806.
- M. J. McAllister, J.-L. Li, D. H. Adamson, H. C. Schniepp, A. A. Abdala, J. Liu, M. Herrera-Alonso, D. L. Milius, R. Car, R. K. Prud'homme and I. A. Aksay, *Chem. Mater.*, 2007, **19**, 4396.
- C. N. R. Rao, K. Biswas, K. S. Subrahmanyam and A. Govindaraj, *J. Mater. Chem.*, 2009, **19**, 2457.
- J. Shen, Y. Hu, M. Shi, X. Lu, C. Qin, C. Li and M. Ye, *Chem. Mater.*, 2009, **21**, 3514.
- S. Stankovich, D. A. Dikin, R. D. Piner, K. A. Kohlhaas, A. Kleinhammes, Y. Jia, Y. Wu, S. T. Nguyen and R. S. Ruoff, *Carbon*, 2007, **45**, 1558.
- R. Guo, L. Zhao and W. B. Yue, *Electrochim. Acta*, 2015, **152**, 338.
- H. G. Wang, Y. H. Wang, Y. H. Li, Y. C. Wan and Q. Duan, *Carbon*, 2015, **82**, 116.
- G. X. Wang, X. P. Shen, J. Yao and J. Park, *Carbon*, 2009, **47**, 2049.
- F. Béguin, F. Chevallier, C. Vix-Guterl, S. Saadallah, V. Bertagna, J. N. Rouzaud and E. Frackowiak, *Carbon*, 2005, **43**, 2160.
- Y. Matsuo and Y. Sugie, *Carbon*, 1998, **36**, 301.
- E. Yoo, J. Kim, E. Hosono, H. S. Zhou, T. Kudo and I. Honma, *Nano Lett.*, 2008, **8**, 2277.
- K. L. Zhang, X. N. Li, J. W. Liang, Y. C. Zhu, L. Hu, Q. S. Cheng, C. Guo, N. Lin and Y. T. Qian, *Electrochim. Acta*, 2015, **155**, 174.
- L. Qie, W. M. Chen, Z. H. Wang, Q. G. Shao, X. Li, L. X. Yuan, X. L. Hu, W. X. Zhang and Y. H. Huang, *Adv. Mater.*, 2012, **24**, 2047.
- Q. Zhu, P. Wu, J. Zhang, W. Zhang, Y. Zhou, Y. Tang and T. Lu, *ChemSusChem*, 2015, **8**, 131.

Table of contents



3D porous aMEGO has been achieved with high SSA and improved electrochemical performance for LIBs.